

Reactive Bond-Order Potential for Modeling SiC Oxidation and Annealing with Interface Defect Dynamics

Yeong Jin Ahn, Yun Ho Lee, Su Hyun Park, Jeong Wook Kim, Cheul Hyun Yoon, Seongjun Kim, Young Jae Park, and Byoung Don Kong*



Cite This: *J. Phys. Chem. C* 2025, 129, 15029–15040



Read Online

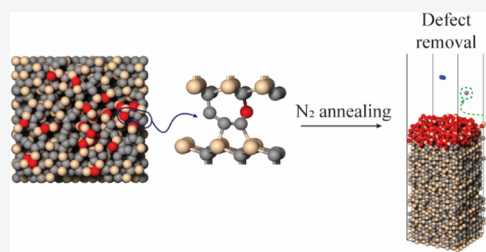
ACCESS |

Metrics & More

Article Recommendations

Supporting Information

ABSTRACT: A newly developed Tersoff-type bond-order potential is presented for molecular dynamics (MD) simulations of silicon carbide (SiC) oxidation and postoxidation annealing processes. The potential encompasses interactions among Si, C, O, N, and H atoms and was parametrized using density functional theory (DFT) calculations, with experimental calibration to ensure predictive accuracy. The potential reliably reproduces key structural and thermodynamic properties of SiC-related compounds, as validated through MD simulations of oxidation and annealing. Simulations of thermal oxidation demonstrated the formation of a SiO₂ layer with density and Si–O bond lengths consistent with theoretical expectations, along with the emergence of interfacial carbon-related defects. N₂ annealing simulations revealed dynamic defect evolution, with increased N₂ pressure accelerating carbon removal and oxygen loss. Notably, elevated pressure conditions led to a significant reduction in the level of C–C bond formation, indicating the potential for defect mitigation through annealing control. Importantly, seven previously unreported defect types were identified at the SiC/SiO₂ interface, which were further classified into 11 unique atomic configurations and characterized using DFT. The simulated defect distribution exhibits strong correlation with experimentally observed interface trap densities, providing insight into fast and deep-level trap formation in SiC devices. This work establishes a robust atomistic modeling framework for realistic simulations of SiC oxidation and annealing and offers new avenues for interface defect engineering in next-generation SiC-based electronics.



INTRODUCTION

Silicon carbide (SiC) is one of the most technologically important wide bandgap semiconductors for the extreme environment such as high voltage and temperature applications due to the high breakdown voltages and high thermal conductivities.^{1–3} A convenient implementation of metal oxide semiconductor field effect transistors (MOSFETs) on SiC is a great advantage for such applications, which stems from the thermal oxidation of SiC and the formation of silicon dioxide (SiO₂).^{4,5} The good physical properties also make it an ideal candidate for high-frequency applications. However, the low mobility stems from the carbon-related oxide defects remain as the hurdle to be overcome.^{6,7} In particular, the C–C bonds formed at the interface during oxidation are known to be the major source of the mobility degradations.⁸ As such, understanding the SiC oxidation process and resulting interface structures is crucial to realize high-performance SiC devices.

Various studies have been conducted using density functional theory (DFT) to predict the oxidation and carbon defects in SiC, such as carbon vacancies and C–C double bond at the interface.^{6,7,9,10} DFT serves as a powerful method in analyzing a physical system with a small number of atoms. However, its application to dynamic processes like oxidation and annealing in macroscopic to mesoscopic systems is clearly

limited due to the demanding computing resources. Molecular dynamics (MD) simulation is ideally suited for simulating dynamic processes with a large number of atoms, which cannot be handled by DFT. However, MD simulation with typical two-body potential describes interactions between atoms only based on distances, making it challenging to realize and analyze realistic structures.

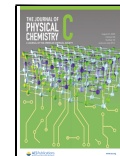
To address such issues, the bond-order potential (BOP) has been developed, with the Tersoff potential recognized as a notable example. Tersoff potential introduces local bond-order and bond-angle dependencies into the Morse-type pair potential,^{11,12} resulting in plausible characterization of solid structures such as silicon, silicon dioxide, and silicon carbide.^{11,13,14} Tersoff potential has successfully reproduced defects and physical parameters in SiC such as the lattice constant and elastic constants.¹² Accordingly, a BOP-based potential for multielement systems including C, O, Si, and additional atoms can enable a realistic modeling of dynamic

Received: May 8, 2025

Revised: August 4, 2025

Accepted: August 4, 2025

Published: August 11, 2025



processes in SiC, such as oxidation, which is difficult to achieve using two-body potentials alone.

This work presents an MD study of SiC oxidation and defect annealing utilizing BOP. A Tersoff-type BOP for multielement systems containing Si, C, O, N, and H was developed, based on atomic binding energies computed by DFT and calibrated to match experimental results. The stability of the potential was tested by room-temperature annealing and phase transition simulations of the compounds composed of Si, C, O, N, and H. Using this potential, SiC oxidation and N₂ annealing to remove interface carbon defects were simulated. It is known that annealing processes incorporating N can reduce the density of interface defects.^{31–34} However, the specific mechanisms involved in defect removal and the defects that occur during the dynamic process of N₂ annealing have still not been sufficiently studied. The carbon defects generated during the simulation were categorized into 11 different structures, and their configurations and energies were calculated by using DFT. The energy distribution of these defects was then analyzed under varying N₂ pressures.

Development of the Molecular Dynamics Potential for the Si-C-O-N-H System. The SiC oxidation and annealing study, as illustrated in Figure 1, was conducted in

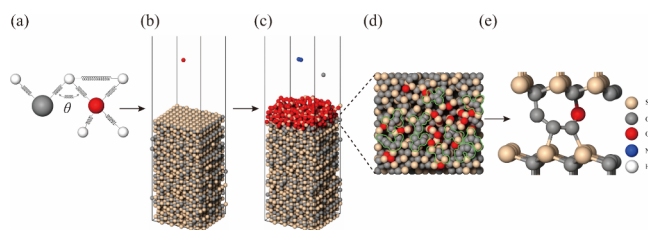


Figure 1. Overall research process. (a) Bond order-dependent interaction, (b) SiC oxidation, (c) N₂ annealing, (d) interface structure after oxidation with carbon-related defects, (e) structure of defects calculated using DFT.

the following order: development of the BOP, MD simulations, and defect analysis. In this study, a Tersoff-type bond-order potential was adopted. This potential accounts for bond-angle dependence and is computationally efficient, making it well suited for large-scale simulations. It enables a physically reasonable description of atomic configurations, particularly in amorphous solid interfaces where a large number of atoms and diverse bonding environments must be handled. This efficiency is particularly advantageous for studying defect structures at

the SiC/SiO₂ interfaces formed during oxidation and annealing. For explicitly reactive processes involving bond breaking and formation, reactive force fields such as ReaxFF are commonly used. ReaxFF includes charge equilibration to dynamically assign partial charges and can describe complex chemical reactions, such as combustion or redox reactions in battery materials. However, this added complexity leads to significantly higher computational costs—of 10 orders of magnitude higher than traditional bond-order potentials like Tersoff, though still far below the cost of density functional theory (DFT). Therefore, the developed Tersoff-type potential offers a practical advantage for modeling solid-state processes at scale, where the focus is on structural and defect evolution rather than detailed chemical reactivity.

Tersoff potential describes three-body interactions based on the distances between atoms (r_{ij}) and angles between them (θ_{ijk}), with indices i , j , and k representing the respective atoms. With a two-element system (A and B), 8 bindings for i , j , and k can be identified. However, the Tersoff potential distinguishes the elements only at i and j . Additionally, due to symmetry, A–B interaction and B–A interactions are equivalent. Thus, there are three identifiable binding cases that require parameter determination in two-element systems: A–A, A–B, and B–B. For a five-element system with Si, C, O, N, and H, there are 15 possible cases: Si–Si, Si–C, Si–O, Si–N, Si–H, C–C, C–O, C–N, C–H, O–O, O–N, O–H, N–N, N–H, and H–H. Actually, the Tersoff parameters for some bindings are already known. Specifically, the parameters for Si–Si, Si–O, Si–C, Si–N, Si–H, O–O, C–C, C–N, N–N, N–H, and H–H bindings were adopted from the literature.^{13–16} The remaining combinations, C–O, C–H, O–H, and O–N, were parametrized and summarized in Table 1. In order to match the predeveloped Tersoff potentials from the literature, the original Tersoff potential model was employed, in which the total energy E is the sum over the energies of all n atoms, indexed by i . As such,

$$E = \sum_{i=1}^n E_i = \frac{1}{2} \sum_{i \neq j}^n V_{ij} \quad (1)$$

where V_{ij} is the interaction energy between atoms i and j . V_{ij} is the combination of repulsive and attractive terms, so that

$$V_{ij} = f_c(r_{ij})[f_R(r_{ij}) + b_j f_A(r_{ij})] \quad (2)$$

where f_R and f_A stand for the repulsive and attractive interactions, which are given as

Table 1. Tersoff Potential Parameters for the Si, C, O, N, and H System^a

	C–O	C–H	O–H	O–N
A	(eV)	6.333×10^3	4.854×10^3	2.052×10^4
B	(eV)	2.047×10^3	1.947×10^3	0.077×10^3
λ	(\AA^{-1})	4.807	5.216	10.24
μ		3.508	4.200	2.714
β		2.264×10^{-6}	1.608×10^{-5}	8.480×10^{-5}
n		0.520	1.206	0.890
c		1.063×10^3	1.500×10^3	1.402×10^3
d		5.567	3.811	5.000
h		-1.00	-1.00	-0.36
R	(\AA^{-1})	2.2	2.2	2.2
S	(\AA^{-1})	2.5	2.5	2.5

^aRemaining parameters are in the references.^{13–16}

$$f_R(r_{ij}) = A_{ij} \exp(-\lambda_{ij} r_{ij}) \quad (3)$$

and

$$f_A(r_{ij}) = -B_{ij} \exp(-\mu_{ij} r_{ij}) \quad (4)$$

f_c is a cutoff function, which goes from 1 to 0 in a small range around R . R is defined to include only the first-neighbor shell. Specifically, f_c is given as

$$f_c(r) = \begin{cases} 1, & r_{ij} < R_{ij} \\ \frac{1}{2} + \frac{1}{2} \cos\left(\pi \frac{r_{ij} - R_{ij}}{S_{ij} - R_{ij}}\right), & R_{ij} < r_{ij} < S_{ij} \\ 0, & r_{ij} > S_{ij} \end{cases} \quad (5)$$

b_{ij} provides bond-order dependence, which reads as

$$b_{ij} = (1 + \beta^n \xi_{ij}^n)^{-1/2n} \quad (6)$$

where

$$\xi_{ij} = \sum_{k \neq i,j} f_c(r_{ik}) g(\theta_{ijk}) \exp[\lambda_3^m (r_{ij} - r_{ik})^3] \quad (7)$$

and

$$g(\theta_{ijk}) = 1 + \frac{c_i^2}{d_i^2} - \frac{c_i^2}{d_i^2 + (h_i - \cos(\theta_{ijk}))^2} \quad (8)$$

Here, $g(\theta_{ijk})$ is the term related to the angular dependence.

Recently, machine learning potentials (MLPs) have been utilized to derive interatomic potential parameters, including Tersoff-type potentials, by training on data sets generated from density functional theory (DFT) calculations. Several studies have also applied MLPs to parametrize Tersoff potentials for multielement systems.^{17–19} In a similar spirit, Tersoff potential parameters were manually derived based on direct DFT calculations and subsequent calibration against experimental data, without relying on large-scale computational training. Furthermore, while neural network potentials represent a promising direction, they essentially perform a black-box fitting of parameters based on the training data. In practice, generating a comprehensive and high-quality DFT data set that spans the full range of relevant atomic configurations for complex multicomponent systems is computationally prohibitive. In contrast, our approach offers a more physically transparent and tractable route to potential development, grounded in both quantum mechanical accuracy and experimental validation.

The DFT calculations were performed by using the SIESTA DFT suite with the local density approximation (LDA) for exchange-correlation energy. While LDA is known to underestimate the band gap, it provides an accurate description of atomic bonding characteristics. Given that molecular dynamics (MD) potentials rely primarily on the accurate description of minimum energy configurations as a function of the bond length, LDA is well suited for this purpose. The precision of bond length and binding energy predictions is critical in developing reliable bond-order potentials, and in this regard, LDA offers a favorable tradeoff compared with more advanced hybrid functionals that prioritize electronic properties over structural fidelity.

It is known that there can be some overestimation in cohesive energies calculated under LDA.²⁰ As such, the

cohesive energies of each structure were adjusted to match the experimental values.²¹ The parametrization was conducted with various structures to encompass a broad range of bond lengths and a diverse number of interacting atoms. This also ensures that the calculated potential parameters are accurate and applicable to a wide range of environments. Calculations were conducted on the dimer, rock salt, simple cubic, and zinc blende structures. For targeted bonding, the binding energy of the dimer was calculated, and the ratio to the experimental value was obtained. The cohesive energies for rock salt, simple cubic, and zinc blende structures were adjusted by using the ratio of the theoretical and experimental values for the dimer. Then, the parameters were fitted to reproduce the structure and binding energies of these structures. Additional details regarding the testing procedure are provided in the Supporting Information.

Comprehensive Stability Evaluation of the Si-C-O-N-H Potential. To verify the accuracy of the developed potential and validate its broad applicability, the stability of materials composed of Si, O, N, and H was conducted under various environmental settings. First, binary gas molecule formation and their stabilities were tested. The MD simulation was performed using Large-scale Atomic/Molecular Massively Parallel Simulator (LAMMPS).²² Three atoms constituting CO₂, NO₂, and N₂O were introduced separately. For instance, Cs and Os were introduced at a 1:2 ratio. All three studied cases, the gas molecules, were successfully formed, and their bond lengths and bond angles remained consistent with known theoretical values, indicating structural stability during the simulation. These simulations were conducted under the NVT ensemble (canonical ensemble) condition at 300 K for 5 ps, with a time step of 0.5 fs, respectively. In the following NPT (isothermal–isobaric ensemble) simulations, preconstructed gas molecules (CO₂, NO₂, and N₂O) were directly inserted into the simulation cell to assess their structural stability. The simulations were conducted for 5 ps of annealing at 300 K with a time step of 0.5 fs. During the simulation, the bond lengths and bond angles of each molecule remained stable and consistent with the known theoretical values. After the binary compounds, a ternary compound, Si₂N₂O crystal, was tested. A Si₂N₂O structure consisting of 200 Si, 200 N, and 100 O atoms was used as the input structure. Annealing was conducted at 300 K under NPT conditions. The input structure was maintained throughout the simulation, and the resulting density was 2.6 g/cm³, which was comparable to the DFT simulation result²³ of 2.82 g/cm³ and the experimental value²⁴ of 2.81 g/cm³.

To evaluate the stability and transferability of the developed potential across chemically diverse systems, simulations involving annealing and phase transitions were performed on molecules with complex bonding characteristics, including adrenaline, serotonin, polydimethylsiloxane (PDMS), and trimethylsilane (3MS). While bulk SiC features predominantly sp³ tetrahedral bonding, interfacial structures can deviate significantly from this configuration due to local disorder and chemical heterogeneity. By applying the potential to molecular systems characterized by sp₂-type bonding, the transferability of the potential—specifically, its ability to stably model a wide range of bond angles and bonding environments—was assessed. The initial structures of these materials were obtained using Avogadro²⁵ and used for the MD simulations. Annealing simulations were conducted for these molecules at 300 K, and the results showed stability at room temperature with density

values similar to the experimental values. Figure 2 shows the molecular structures that remained stable after annealing, and

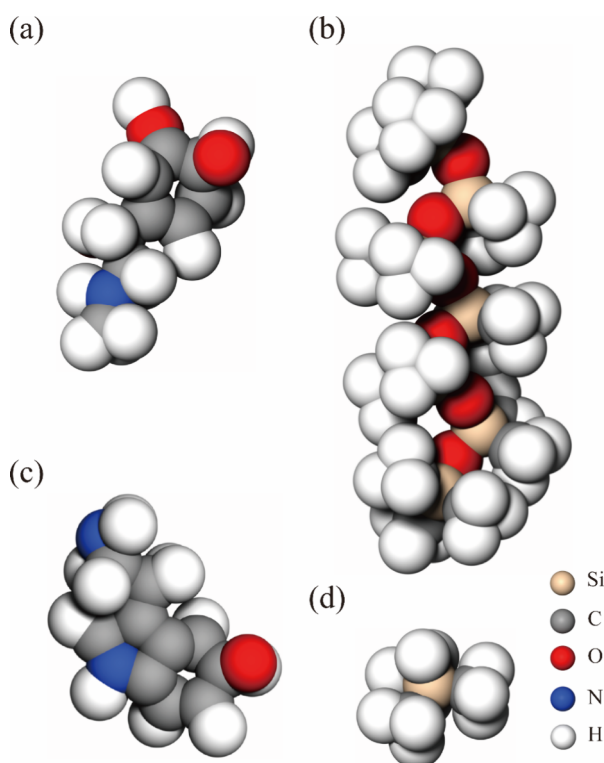


Figure 2. Molecules after stability test: (a) adrenaline, (b) PDMS, (c) serotonin, and (d) 3MS.

Table 2. Stability Test Simulation Results of Adrenaline, Serotonin, 3MS, and PDMS^a

	simulation results	experimental value
adrenaline	1.3 g/cm ³	1.331 g/cm ³
serotonin	1.2 g/cm ³	1.3 g/cm ³
3MS	0.7 g/cm ³	0.638 g/cm ³
PDMS	0.8 g/cm ³	0.97 g/cm ³

^aThe density of serotonin was predicted using the ACD/Laboratories Percepta Platform—PhysChem Module. Other experimental values were obtained from reference sources.^{45–47}

the experimental and simulation results are listed in Table 2. For PDMS ($\text{CH}_3[\text{Si}(\text{CH}_3)_2\text{O}]_n\text{Si}(\text{CH}_3)_3$), simulations were conducted using five repeating units of $\text{Si}(\text{CH}_3)_2\text{O}$. The annealing simulations were conducted under the NPT ensemble condition at 300 K using the Nose-Hoover style non-Hamiltonian equations of motion.^{26,27} The simulations were performed for a total of 5 ps with a time step of 0.5 fs.

Next, phase transition simulations for PDMS and trimethylsilane (3MS) were conducted. For 3MS, the simulations were performed using 10 molecules, with temperature increased while observing density, volume, and potential energy. 3MS was heated from 10 to 500 K, and the melting point and boiling point were determined using the ref 28 method. For PDMS ($\text{CH}_3[\text{Si}(\text{CH}_3)_2\text{O}]_n\text{Si}(\text{CH}_3)_3$), the simulation was conducted with 50 repeating monomer units of $\text{Si}(\text{CH}_3)_2\text{O}$ and the temperature was increased from 100 to 1000 K. The melting point of PDMS was determined using the

same method applied for calculating the melting point of 3MS, while the glass transition temperature was obtained following the approach outlined in ref 29. To determine glass transition temperature, the system was cooled from 300 to 50 K. The simulations were conducted under the NVT ensemble condition using the Nose-Hoover style non-Hamiltonian equations of motion,^{23,24} and they were performed for a total of 2.5 ps with a time step of 0.5 fs. The phase transition results of 3MS and PDMS are listed in Table 3. Combining the calculated results, the Tersoff potential demonstrated clear advantages in realistic MD simulations.

Table 3. Phase Transition Simulation Results of 3MS and PDMS^a

molecule	phase	simulation results	theoretical value
3MS	melting	150 K	137.15 K
3MS	boiling	330 K	279.85 K
PDMS	melting	230 K	230.15 K
PDMS	glass transition	150 K	123.15 K

^aExperimental values were obtained from reference sources.^{48–50}

SiC Oxidation and Nitrogen Annealing Simulations.

a. Oxidation. The results of the oxidation simulation using the developed potential are shown in Figure 3. The simulation was conducted on the 4H-SiC Si(001) face, with the initial size of 3280 atoms' bulk silicon carbide of $24.6 \times 24.0 \times 50.4 \text{ \AA}$. The simulation size was chosen to balance computational efficiency, allow detailed analysis of the interface structure, and maintain structure stability. The boundaries along the X and Y directions were set to be periodic, while the boundaries along the Z direction were set as reflecting. The bottom-layer atoms were fixed by assuming that there is a SiC substrate below them. The time step was set to 0.5 fs, and oxygen atoms were added every 7.5 ps, with the simulation running for a total of 3.75 ns. Oxygen atoms were inserted into the region between $Z = 70 \text{ \AA}$ and $Z = 100 \text{ \AA}$, ensuring sufficient spacing to minimize oxygen–oxygen collisions and allow uniform injection dynamics. The simulation was conducted at 2000 K by using an NVT ensemble to accelerate the oxidation process. While the actual oxidation time scale can extend to several hours, molecular dynamics simulations are limited by computational constraints. The choice of 2000 K was further supported by the Tersoff potential, which predicts a higher melting point for SiC than the experimental values, ensuring structural stability during simulations. At this elevated temperature, oxidation dynamics were effectively observed with oxygen atoms introduced into the simulation domain at an initial velocity corresponding to 2000 K, mimicking realistic thermal conditions. The simulation results show that a total of 1.1 Å thick SiO_2 layer was formed by consuming 0.5 Å of SiC, with the theoretical consumption rate being approximately 0.45 Å of SiC per 1 Å of SiO_2 .³⁰ The constructed oxide contained 159 Si and 316 O atoms, roughly satisfying a 1:2 ratio for SiO_2 . The radial distribution function (RDF) of Si–O, as shown in Figure 3d, has a peak value at 1.7 Å, which is similar to the bond length of SiO_2 .^{31,32} Additionally, as illustrated in Figure 3c, C–C bonding, C clusters, and C defects involving carbon bonding with other atoms were generated at the interface. The RDF of C–C bonding at the interface, shown in Figure 3e, shows the peak values at 1.5 Å, which is similar to the bond length of C–C defects that can occur during the oxidation of SiC.⁹ The oxidation simulation

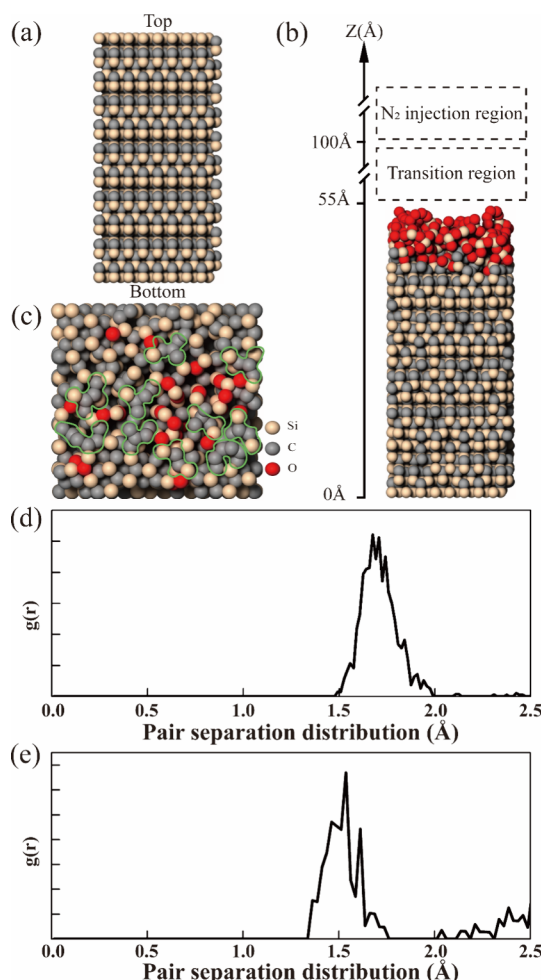


Figure 3. (a) Initial structure before oxidation process; (b) structure after oxidation process, positional N₂ annealing simulation; (c) interface structure, with the highlighted areas indicating carbon defects; (d) Si–O radial distribution function; (e) interface C–C radial distribution function.

results show that the developed potential successfully produced a realistic oxidized SiC structure.

b. N₂ Annealing. The N₂ annealing process was performed on the previously formed oxide to analyze the C defect removal process macroscopically. The initial structure for annealing is shown in Figure 3a, with the SiC substrate located at the bottom. After the oxidation process, as illustrated in Figure 3b, the SiO₂ layers formed above the SiC substrate, spanning a total height of 55 Å as indicated in the figure. The area from 55 to 100 Å is the transition region, and the area above 100 Å is the N₂ injection region. The transition region was set to observe atomic reactions. The N₂ injection region also played the role of removing emitted particles from the oxide, where any atoms or molecules that reached the region were eliminated using the “evaporate” command. In the N₂ injection region, the number of N₂ molecules was maintained at 1, 2, 3, 4, and 5 for the 1, 2, 3, 4, and 5 bar conditions, respectively. The top boundary of this region was adjusted according to the ideal gas law to ensure that the injected N₂ density matched the desired pressure. If the number of N₂ molecules fell below the target value, then additional N₂ molecules were injected from the top of the region. Since the diffusion coefficient of oxygen is higher than that of

nitrogen, excessively high temperatures could lead to additional oxidation. To prevent this, the simulation was conducted at 2000 K, at which the oxidation was performed using the Nose-Hoover style non-Hamiltonian equations under NVT conditions. Injected N₂ molecules were assigned initial velocities corresponding to the thermal velocity at 2000 K. In the preannealing simulation without N₂, the SiC–SiO₂ composition and the structure were stable, showing that the interface carbon removal is hard to occur without N₂.

In the N₂ annealing, the changes in C–C bonding were analyzed under different N₂ pressures along with the reduction of C at the interface, oxygen loss, reaction types, and final interface forms. The N₂ pressure was set at 1, 2, 3, and 4 bar, and the simulation was run for 15 ns with a 0.5 fs time step. Figure 4 shows the time evolution of both the number of C–C bonds (black line) and the number of carbon atoms at the interface (red line) under varying N₂ pressures. The simulation started with 45 C–C bonds, and at all studied pressures, the number of C–C bonds was increased for the initial 9 ns.

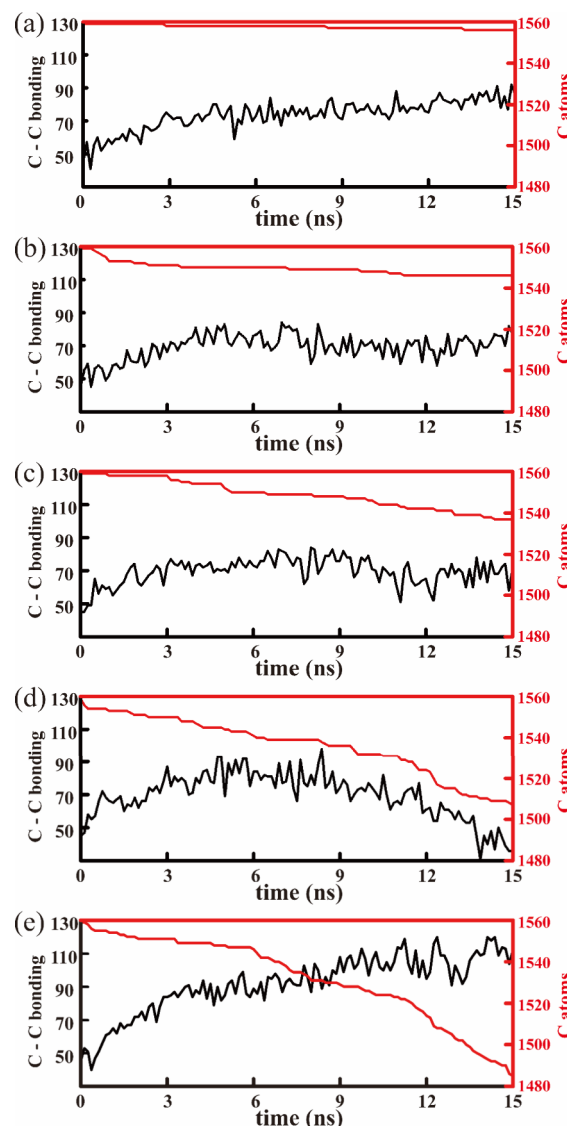


Figure 4. Graph of C–C bonding count (black) and the number of total carbon atoms (red) as a function of N₂ flow rate: (a) 1 bar, (b) 2 bar, (c) 3 bar, (d) 4 bar, and (e) 5 bar.

Table 4. Simulation Results of Annealing Under Different N₂ Pressures^a

N ₂ pressure	removed atoms		initial state + reactive gas				emission type		
	carbon	oxygen	single C + O	C cluster + O	single C + N	C cluster + N	C	CO	CN
1 bar	3	34	0	3 (100%)	0	0	0	3	0
2 bar	13	66	5 (38.5%)	1 (7.69%)	3 (23.1%)	4 (30.8%)	3	9	1
3 bar	23	91	9 (39.1%)	2 (8.70%)	7 (30.4%)	5 (21.7%)	18	2	3
4 bar	53	152	16 (30.2%)	12 (22.6%)	13 (24.5%)	12 (22.6%)	31	20	2
5 bar	74	212	19 (25.7%)	24 (32.4%)	22 (29.7%)	9 (12.2%)	44	22	8

^aOn the left, the number of removed carbon and oxygen atoms is displayed. In the middle, the count is categorized by initial state + reactive gas, with the number in parentheses indicating the proportion of carbon removed via initial state + reactive gas out of the total removed carbon. On the right, the count is based on the emission form of the removed carbon.

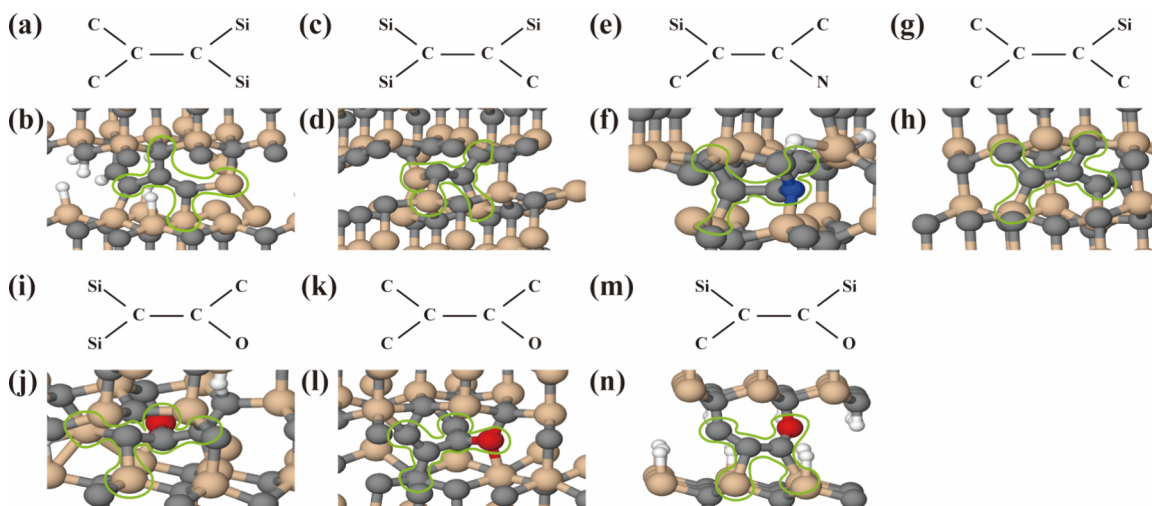


Figure 5. Schematics and corresponding atomic structures. Panels (a,b) correspond to (C₂)-C-C-(Si₂); panels (c,d) correspond to (Si₂)-C-C-(SiC); panels (e,f) correspond to (SiC)-C-C-(CN); panels (g,h) correspond to (C₂)-C-C-(SiC); panels (i,j) correspond to (Si₂)-C-C-(CO); panels (k,l) correspond to (C₂)-C-C-CO; panels (m,n) correspond to (SiC)-C-C-(SiO).

Afterward, the trend displayed a drastic difference as a function of the pressure. Specifically, the number continued to increase at 1 bar, while at 4 bar, the number of C–C bonds started decreasing. In contrast, the trends at 2 and 3 bar were relatively stable. At 2 bar, the number of C–C bonds showed a slight decrease immediately after 9 ns, with an average of 69.1 bonds between 9 and 12 ns, followed by a small increase to an average of 71.2 bonds between 12 and 15 ns. At 3 bar, the number of C–C bonds slightly decreased throughout the simulation from 9 to 15 ns, with an average of 69.4 bonds between 9 and 12 ns and 67.6 bonds between 12 and 15 ns. As the results, the final numbers of C–C bonds were 86, 77, 71, and 36 for 1, 2, 3, and 4 bar, respectively. Intriguingly, it was found that the decrease of C–C bonds started sharply expediting in the later stages of the simulation at 4 bar, which suggests that the supplied N₂ effectively breaks the C–C bonds and contributes in removing redundant carbon from the interface efficiently at the pressure greater than 4 bar. The details of this process will be further elaborated on in the subsequent analysis. One drawback of the C removal at the elevated pressure is the accompanied high oxygen loss. For instance, as the pressure increased from 3 to 4 bar, a significant reduction of the carbon at the interface was observed (from 23 to 53), while a significant oxygen loss was also accompanied (from 91 to 152), as summarized in Table 4 and Figure 4. This implies that N₂ annealing can effectively eliminate interfacial carbon defects at 4 bar. Based on these observations, an additional simulation was conducted at 5 bar to investigate

how the interfacial carbon removal and oxygen loss evolve with further increase in N₂ flow rate and to examine the behavior of C–C bonds under this flow rate. At 5 bar, the number of removed carbon atoms further increased to 74. Although the removal of interface carbon increased further, the number of C–C bonds increased instead of decreasing. This suggests that an excessive N₂ supply may promote recombination of remaining carbon atoms, leading to increased C–C bonding despite overall carbon loss. The final number of C–C bonds had decreased from 1 to 4 bar but increased again to 144 at 5 bar. The oxygen loss reached 212, continuing the increasing trend with the N₂ flow rate. These results indicated that although interfacial carbon removal and oxygen loss both increased with an increasing N₂ flow rate, in terms of C–C bonding, it initially decreased with increasing N₂ flow rate and reached a minimum at 4 bar but then increased again at 5 bar. Therefore, there must be an optimal point to balance effective carbon removal with the suppression of oxygen loss and C–C bond formation. The interface carbons were released from the oxide surface in the forms of C, CO, and CN. The number of removed C and O atoms, the reaction types, the type of removed carbon, and the emitted forms are summarized in Table 4. The quantity of carbon released as CO increased from 2 to 20 at 4 bar, further to 22 at 5 bar, which appears to be the major mechanism of the carbon removal. At the same time, it inherently accompanies the significant increase in oxygen loss. The amount of interface carbon atoms removed as CN remained below 8 at all N₂ pressures.

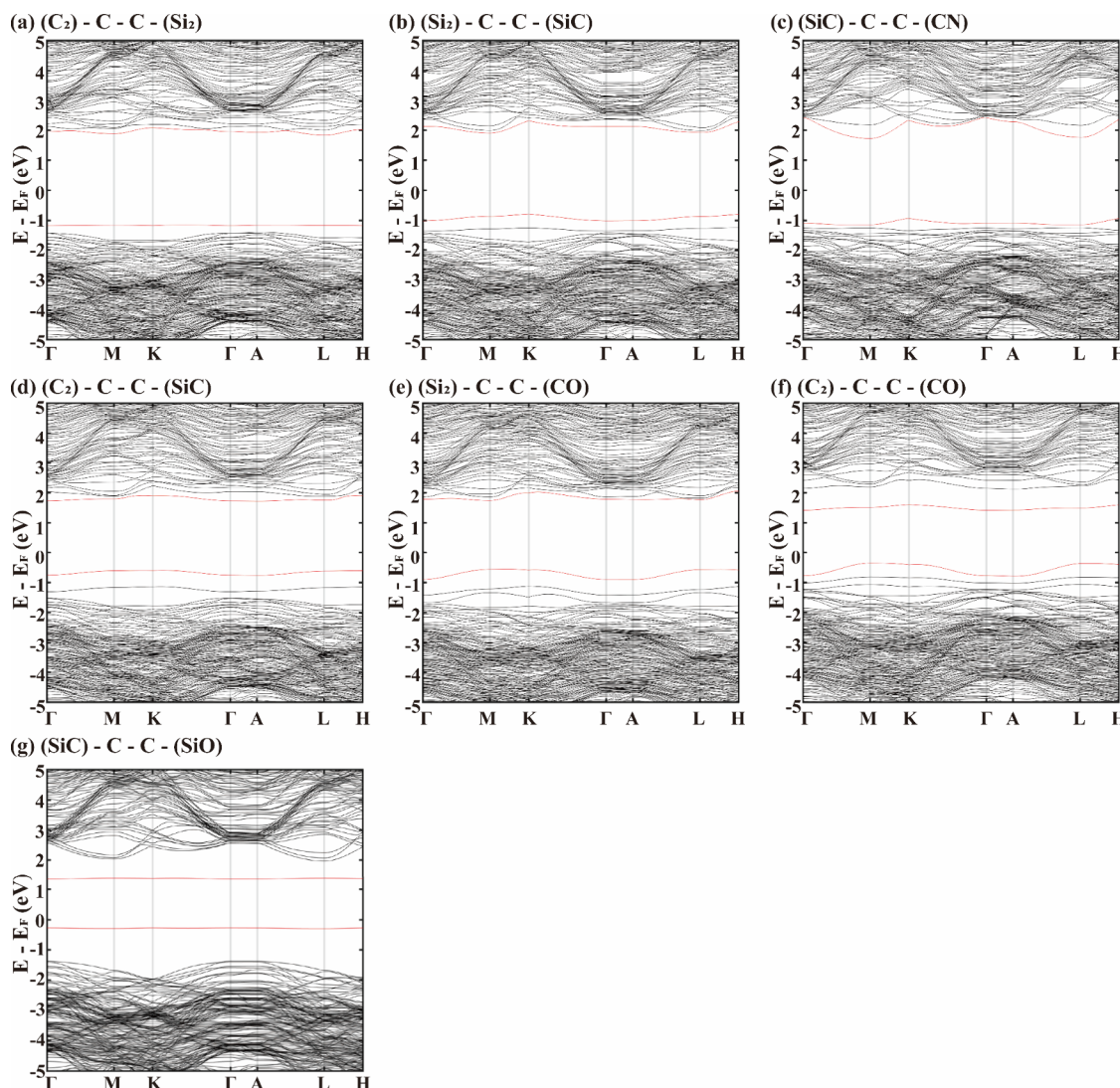


Figure 6. Band structure of defects. The defect band was indicated with a red line. (a) (C_2) -C-C-(Si_2). (b) (Si_2) -C-C-(SiC). (c) (SiC) -C-C-(CN). (d) (C_2) -C-C-(SiC). (e) (Si_2) -C-C-(CO). (f) (C_2) -C-C-(CO). (g) (SiC) -C-C-(SiO).

To further analyze the N_2 annealing process, the types of removed carbon were classified based on the number of attached carbons. The proportion of single-carbon removal was found to be 0, 61.6, 69.5, 54.7, and 55.4% at 1, 2, 3, 4, and 5 bar, respectively. As such, the removal of the single atom form increases as the pressure is elevated but starts decreasing at 4 bar and showed a slight increase again at 5 bar. The ratios of the removal by a cluster were 38.4 and 30.4% at 2 and 3 bar, among which 30.8 and 21.7% were removed by reacting with nitrogen ($\text{N}-\text{C}$ cluster), while the remaining reacted with oxygen ($\text{O}-\text{C}$ cluster). This clearly indicated that nitrogen reactions were more favored for the removal of carbon clusters. At 4 bar, the ratios of carbon clusters reacted with nitrogen and oxygen were nearly identical, and at 5 bar, reactions with oxygen exceeded those with nitrogen, which can also be related to the substantial oxygen loss at 4 bar and its further increase at 5 bar. The reaction types can also be classified by the element that the removed carbons bonded to before its release. The ratios of carbon removed through nitrogen were 0, 53.9, 52.1, 47.1, and 41.9% at 1, 2, 3, 4, and 5 bar, respectively, while the others were removed through oxygen. This suggests that the increase in oxygen-related reactions at higher pressure is more

strongly attributed to the elevated oxygen loss rather than the increase in N_2 flow rate.

c. Defect Energy Level. Since the structure with carbon atoms in the oxide works as defects,³⁶ whose energy levels exist within the energy gap of SiO_2 , the energy levels of the carbon-related defects identified during the annealing MD simulation were calculated using DFT. At first, the defect structures were categorized from the MD simulations as follows. C-C bonds with lengths below 1.5 Å were identified as defect centers. Next, based on the defect structures identified in a previous DFT study,⁹ the corresponding structures were examined in the MD simulation results. Specifically, the defect structures were determined as six-atom units consisting of a C-C pair and the two nearest neighboring atoms attached to each C atom. A total of 11 types of defects were identified from the simulation, but 4 of them (Si_2 -C-C- Si_2 , C_2 -C-C- C_2 , CSi-C-C-CSi, and CSi-C-C-SiC) were known previously, whose energy levels were actively studied. Thus, the energy levels of the newly identified defects illustrated in Figure 5 were calculated using DFT and the results are shown in Figure 6. The DFT calculations were performed using the SIESTA DFT suite,³⁷ under the local-density approximation (LDA) for the

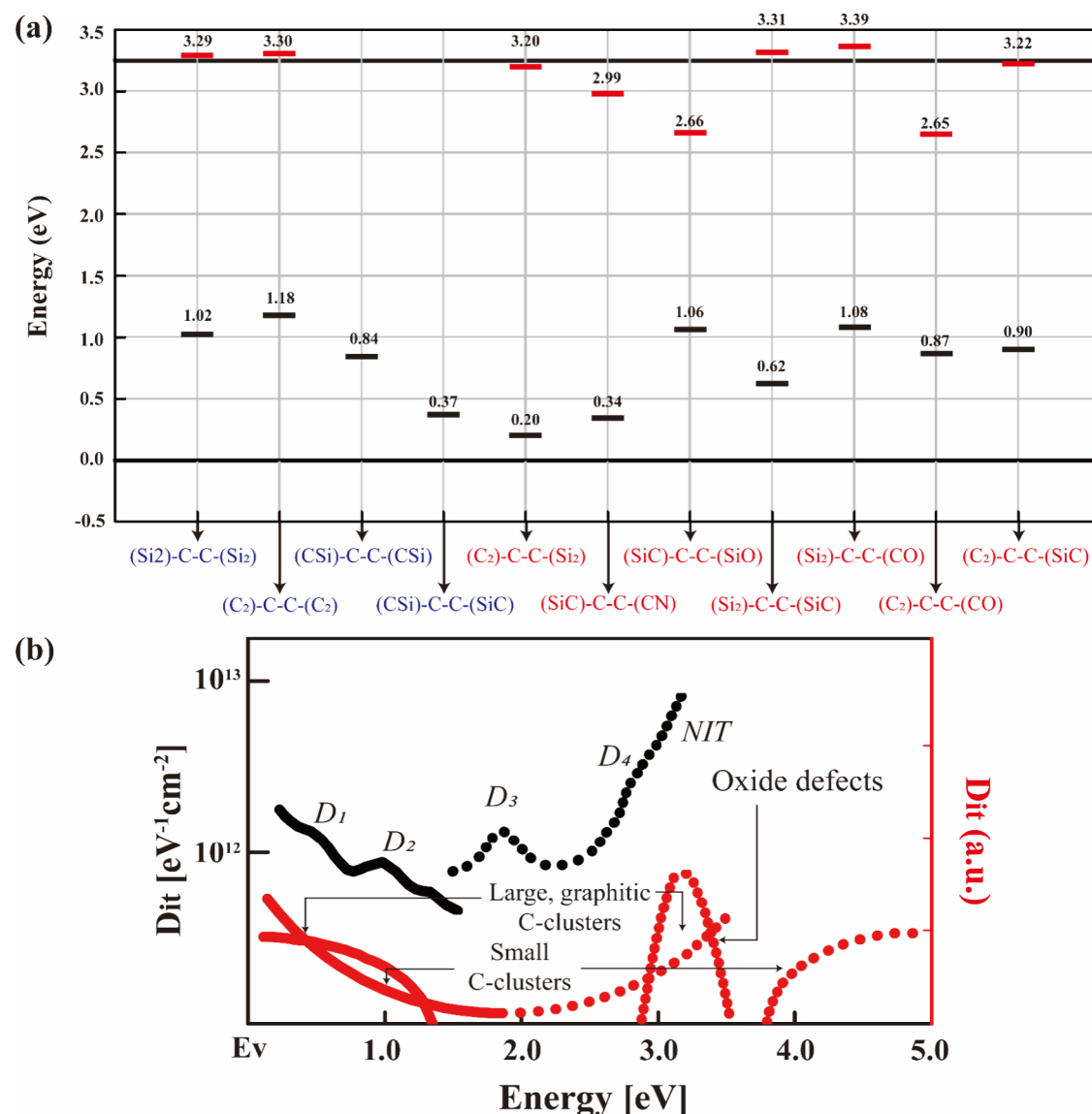


Figure 7. (a) Energy levels within the bandgap of SiC for different defect types, with the bulk valence band maximum set to 0 eV and the conduction band minimum set to 3.25 eV. Energy levels from ref 9 are marked in blue, and newly identified defects from this study are marked in red for clarity. (b) Schematic overview of the experimental data on the D_{it} at the 4H-SiC/SiO₂ interface and the carbon cluster model for explanation of the D_{it} .⁴⁴

exchange-correlation energy. The pseudo potentials used were the optimized norm-conserving pseudopotentials in the Troullier-Martins form, suitable for the LDA approach.³⁸ The mesh cutoff of 100 Ry was chosen to minimize the energy of the bulk structure. Although hybrid functionals yield bandgaps close to experimental values, the inclusion of nonlocal exchange can introduce challenges in accurately describing localized defect states. The mixing coefficient in hybrid functionals varies by system,³⁹ and the optimal value for bulk bandgap correction may not align with that for defect state calculations.^{40,41} Therefore, due to this limited transferability, hybrid functionals are unsuitable for accurately describing the amorphous structures resulting from the N₂ annealing MD simulations. Moreover, the exact exchange term diverges at short distances,³⁹ potentially leading to numerical instability and increasing the complexity of defect state predictions. While hybrid functionals provide improved bandgap estimations, this does not necessarily guarantee a

more precise description of defect energy levels.³⁹ Moreover, their use of different Hamiltonians for short- and long-range interactions⁴² can introduce inconsistencies in the orthonormality of electronic states, which may influence the accuracy of defect state calculations. To address these challenges and ensure consistent and reliable predictions, we chose LDA as a more stable and transferable framework for defect calculations, ensuring reliable descriptions of localized defect states while mitigating the uncertainties associated with hybrid functionals. The defect energy levels were calculated by inserting the defect structures into a bulk SiC system containing 144 atoms, where one layer of Si and one layer of C atoms were removed from the center. The band structures of the bulk and the defect-containing systems were then overlaid to identify the conduction band, the valence band, and the defect energy levels. Local density of states (LDOS) was used to confirm whether the energy levels observed between the conduction and valence bands were indeed induced from the C–C cluster

Table 5. Distance and Angle Parameters of the Defects^a

	central C-C bond	A–carbon	B– carbon	C– carbon	D– carbon	A– carbon–B	C–carbon–D
(C ₂)–C–C–(Si ₂)	1.37	1.49	1.50	1.86	1.82	119	107
(Si ₂)–C–C–(SiC)	1.46	1.77	1.87	1.79	1.57	105	129
(SiC)–C–C–(CN)	1.47	1.78	1.53	1.53	1.48	130	110
(C ₂)–C–C–(SiC)	1.39	1.43	1.39	1.77	1.38	124	123
(Si ₂)–C–C–(CO)	1.46	1.85	1.93	1.48	1.49	107	108
(C ₂)–C–C–(CO)	1.43	1.30	1.40	1.35	1.41	123	126
(SiC)–C–C–(SiO)	1.38	1.92	1.43	1.92	1.38	112	115

^aThe structures are labeled according to Figure 5. Based on the central carbon– carbon bond, the atoms bonded to the left carbon atom are designated as A and B, while the atoms bonded to the right carbon atom are labeled as C and D; the expression can be represented as (AB)–C–C–(CD). Distances are given in [Å] and angles are given in °.

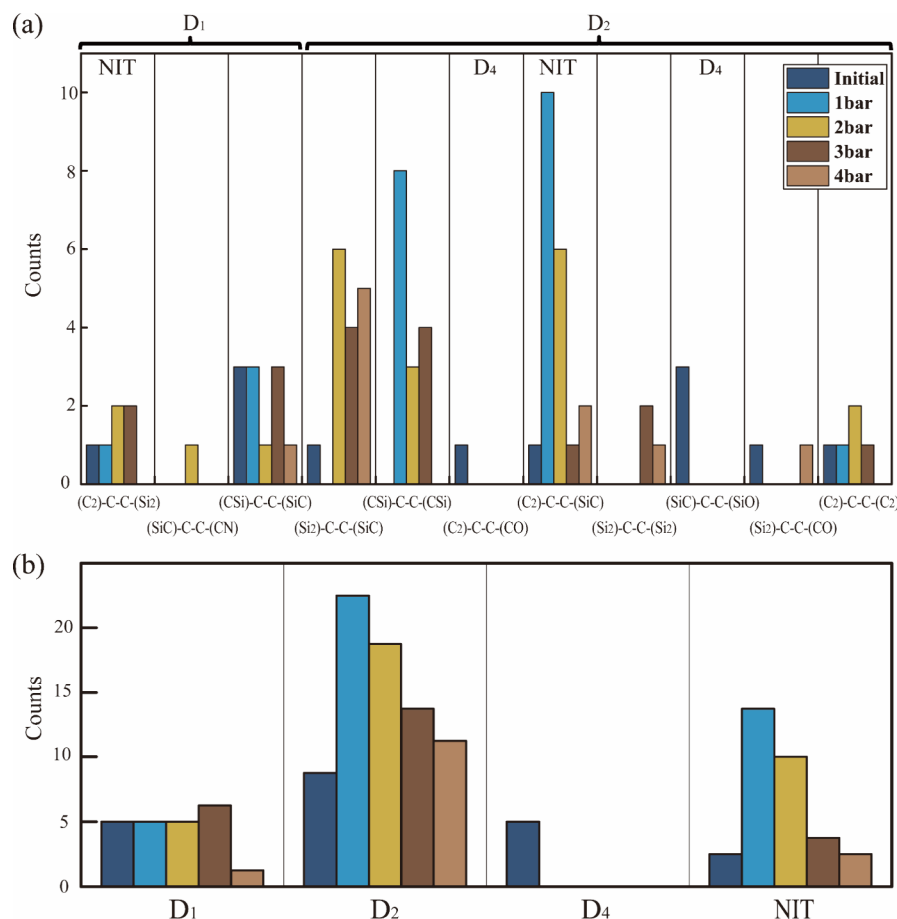


Figure 8. Distribution graph of the number of defects by type according to N_2 pressure: (a) individual defect types, (b) grouped by D_{it} peaks (D_1 , D_2 , D_4 , and NIT).

defects. If it is not induced by the C–C clusters, hydrogen termination was applied to the regions responsible for the bands, allowing defect-induced band structures to be obtained. Furthermore, the projected density of states (PDOS) for 6 atoms within each defect were analyzed to determine if they contributed to the lowest conduction band and the highest valence band. Since LDA tends to underestimate the band gap,⁴³ a scissor operator was applied to adjust the band gap to the value of 3.25 eV from ref 9.

Figure 7a summarizes the energy distributions from the studied C–C cluster defects. The C–C defect clusters are typically in the form of two incomplete tetrahedral bondings facing each other. In other words, in $(\alpha\beta)\text{-C-C-(}\gamma\delta\text{)}$, $(\alpha\beta)\text{-C-C}$ forms an incomplete tetrahedral shape with one corner atom missing, and $\text{C-C-(}\gamma\delta\text{)}$ does the same. As such, there are two

unpaired bondings which could yield two defects states. Indeed, the calculated seven defect clusters showed two defect energy levels, represented by the red lines in Figure 5c,f,i,j,o,r,u: one donor-like state near the conduction band and the other acceptor-like state near the valence band. Among the seven calculated defects, Si₂–C–C–SiC and Si₂–C–C–CO showed their donor-like states above the lowest conduction band when it was analyzed using PDOS. The other five C–C clusters showed their donor-like and acceptor-like states within the SiC band gap. From the PDOS analysis, the donor-like states of those two, along with SiC–C–C–CN, contributed less than 4% of the total DOS, and the energy dispersions did not look like localized defects: they are not flat. Thus, these bands were excluded in the following discussion. In general, the defects containing oxygen formed relatively deep trap levels,

meaning that their energy levels were placed near the center of the band gap.

For a comparison, the experimentally measured density of the interface defects (D_{it}) is shown in **Figure 7b** as a function of energy.⁴⁴ The measured D_{it} graph increases toward the band edges and can be divided into five distinct peaks (D_1 , D_2 , D_3 , D_4 , and NIT, near interface trap). The D_1 peak, located at $E_v + 0.34$ eV, represents shallow-level defects near the valence band and is associated with hole trapping. It is attributed to sp^2 -hybridized carbon structures and carbon dimer defects.⁶ The D_2 peak is located at $E_v + 0.9$ eV, corresponding to deeper trap levels within the bandgap and is primarily linked to carbon interstitials and split interstitial configurations.⁶ The D_3 peak, situated at $E_v + 1.8$ eV, represents deep-level traps in the midgap region and is associated with complex carbon-related defects, including interstitial-vacancy pairs and π -bonded structures.⁶ The D_4 peak, appearing at $E_v + 2.7$ eV, reflects another deep-level state near the upper bandgap edge and is attributed to Si interstitials and their related defects.⁶ Finally, the NIT, located at $E_c - 0.1$ eV, corresponds to interface-related defects near the conduction band, including carbon dimers and silicon-related defects formed during oxidation.⁶ Although the peaks were roughly attributed to specific origins, the precise microscopic structure underlying each peak was not thoroughly analyzed or explicitly discussed.

One tangible outcome of the larger-scale MD study enabled by the developed BOP is the obtained new C–C cluster structures. The identified defects were matched with the experimentally observed D_{it} peaks based on their energy levels. For the D_1 peak ($E_v + 0.34$ eV), defects (CSi)-C-C-(SiC), (C_2)-C-C-(Si_2), and (SiC)-C-C-(CN) were identified. For the D_2 peak ($E_v + 0.8$ eV), a broader set of defects were identified, which are (Si_2)-C-C-(Si_2), (CSi)-C-C-(CSi), (SiC)-C-C-(SiO), (Si_2)-C-C-(SiC), (Si_2)-C-C-(CO), (C_2)-C-C-(CO), and (C_2)-C-C-(SiC). Additionally, a shoulder observed adjacent to the D_2 peak was attributed to (C_2)-C-C-(C_2). The D_4 peak ($E_v + 2.7$ eV) was matched to those of (SiC)-C-C-(SiO) and (C_2)-C-C-(CO). Lastly, the NIT region ($E_c - 0.1$ eV) was linked to the defects (C_2)-C-C-(Si_2) and (C_2)-C-C-(SiC). Additionally, the structural parameters of these defects are summarized in **Table 5**. No defects corresponding to the D_3 peak ($E_v + 1.8$ eV) were observed in the current MD simulations. As previously noted, this peak is associated with interstitial-vacancy pairs and π -bonded structures.⁶ It is likely that a larger-scale simulation incorporating strain, which can facilitate the formation of interstitial-vacancy configurations, would be necessary to generate these defects.

d. Defect MD Results Analysis. **Figure 8** illustrates the changes in defect counts during N_2 annealing at pressures of 1, 2, 3, 4, and 5 bar. **Figure 8a** shows the distribution of individual defect types; **Figure 8b** shows the total number of defects corresponding to each D_{it} peak. Initially, the total number of defects was 12, and after 15 ns of annealing, the number of defects was 23, 21, 17, 10, and 26 for 1, 2, 3, 4, and 5 bar, respectively. As previously described in b, N_2 annealing, up to 3 bar, no decrease in C–C bonding was observed, indicating that the released N_2 pressure was not sufficient. The reduction in C–C bonding started at 4 bar, demonstrating that N_2 molecules operated favorably in C–C defect removal. At 5 bar, the interfacial carbon was further reduced but C–C bonding increased and the total number of defects also increased. To further understand the added N_2 molecule effect, the changes in the total number of defects for each D_{it} peak were analyzed,

followed by an investigation of which components contributed to these variations.

The total number of (CSi)-C-C-(SiC), (C_2)-C-C-(Si_2), and (SiC)-C-C-(CN), which are responsible for D_1 peak, was 4, and it was changed to 4, 4, 5, 1, and 5 at 1, 2, 3, 4, and 5 bar, respectively. These changes were primarily driven by the defects (CSi)-C-C-(SiC) and (C_2)-C-C-(Si_2), which significantly contributed to the overall trend of the D_1 peak. The initial number of defects (CSi)-C-C-(SiC) was 3, and it was observed as 3, 3, 3, 1, and 2 at 1, 2, 3, 4, and 5 bar, respectively. Similarly, the initial number of the defect (C_2)-C-C-(Si_2) was 1, and it was observed as 1, 2, 2, 0, and 3 at 1, 2, 3, 4, and 5 bar, respectively. In contrast, (SiC)-C-C-(CN) contributed minimally to the D_1 peak, appearing only once at 2 bar.

The total number of (Si_2)-C-C-(Si_2), (CSi)-C-C-(CSi), (SiC)-C-C-(SiO), (Si_2)-C-C-(SiC), (Si_2)-C-C-(CO), (C_2)-C-C-(CO), and (C_2)-C-C-(SiC), responsible for D_2 peak, was initially 7 and became 18, 15, 11, 8, and 20 at 1, 2, 3, 4, and 5 bar, respectively. The main contributors were (C_2)-C-C-(SiC) and (CSi)-C-C-(CSi) and (Si_2)-C-C-(SiC). The initial numbers of (C_2)-C-C-(SiC) were initially 1 and became 10, 6, 1, 2, 7 at 1, 2, 3, 4, and 5 bar, respectively. Similarly, (CSi)-C-C-(CSi) was initially 0 but became 8, 3, 4, 0, and 3 at 1, 2, 3, 4, and 5 bar, respectively. (Si_2)-C-C-(SiC) was initially 1 and became 1, 6, 4, 5, and 8 at 1, 2, 3, 4, and 5 bar, respectively. These three defects contributed significantly to the overall increase in D_2 -related defects at 1, 2, and 5 bar. Conversely, (SiC)-C-C-(SiO) and (C_2)-C-C-(CO) were completely removed after N_2 annealing, and (Si_2)-C-C-(CO), whose initial number was 1, was observed only at 4 bar. This indicates that the defects containing oxygen have a minimal contribution to the D_2 peak among the categorized.

The shoulder adjacent to the D_2 peak ($E_v + 1.2$ eV) corresponds to a single defect type, (C_2)-C-C-(C_2), which was initially 1 and became 1, 2, 1, 0, and 1 at 1, 2, 3, 4, and 5 bar, respectively. Actually, this defect demonstrated temporal stability at low pressure, with a slight increase at 2 bar, but remained below 1 at higher pressures.

The initial number of (SiC)-C-C-(SiO) and (C_2)-C-C-(CO), responsible for the D_4 peak, is four: three (SiC)-C-C-(SiO) and one (C_2)-C-C-(CO). Both defects' acceptor-like states also contribute to the D_2 peak, and they share common characteristics with the defects containing oxygen. All defects were reduced under all investigated pressure conditions. These defects have energy levels near the center of the bandgap, which correspond to deep-level states with the energy level difference greater than 0.5 eV from both band edges ($E_c - E$ and $E - E_v > 0.5$ eV). This observation aligns with prior studies indicating that deep-level D_{it} states characterized by $E_c - E > 0.5$ eV decrease significantly during N_2 annealing, suggesting that N_2 annealing is effective in the removal of deep-level defects such as (SiC)-C-C-(SiO) and (C_2)-C-C-(CO).³⁵

Initially, the total number of (C_2)-C-C-(Si_2) and (C_2)-C-C-(SiC), responsible for the NIT, was two: one of each (C_2)-C-C-(Si_2) and (C_2)-C-C-(SiC). After the annealing, the total number was 11, 8, 3, 2, and 10 at 1, 2, 3, 4, and 5 bar, respectively. Both defects's donor-like states contributed to the NIT, while the acceptor-like states contributed to other defect peaks. (C_2)-C-C-(Si_2) contributed to the D_1 and (C_2)-C-C-(SiC) to the D_2 peak. They also exhibited different trends during the N_2 annealing. (C_2)-C-C-(SiC) showed a significant increase from 1 to 2 bar, while remaining constant up to 4 bar, and then increased again to 10 at 5 bar. In contrast, (C_2)-C-C-

(Si₂) showed a slight increase from 2 to 3 bar while being completely removed at 4 bar and then slightly increased to 3 at 5 bar. The main contributor to the NIT was (C₂)-C-C-(SiC), which showed an increase during N₂ annealing except at 3 bar. This result was favorably compared with the previous experimental studies that N₂ annealing increases fast traps at shallow levels in the 4H-SiC/SiO₂ interface.³⁵

CONCLUSIONS

In summary, this study presents Tersoff-style BOP parameters for the Si-C-O-N-H system to enable macroscopic oxidation and annealing simulations of silicon carbide-related materials. Using the developed potential, the stability and phase transition behavior of organic molecules composed of five types of atoms were studied, demonstrating the stability and wide applicability of the developed potential. The following MD simulations for the SiC oxidation and N₂ annealing resulted in the identification of seven new interface carbon defects, along with the microscopic analysis of the defect evolution under N₂ environment. The energy levels analyzed by DFT calculations were compared to the peaks in the experimental D_{it} graph and demonstrated that the developed potential can be utilized in a realistic analysis of the SiC oxidation process. In addition, potential candidates responsible for the fast traps and deep-level defects that align with the experimental observation from N₂ annealing were identified, further validating the developed potential. As such, this study highlights a new pathway for advancing SiC-based technologies.

ASSOCIATED CONTENT

Supporting Information

The Supporting Information is available free of charge at <https://pubs.acs.org/doi/10.1021/acs.jpcc.Sc03173>.

Detailed simulation parameters for MD simulations and detailed testing procedure of potential development ([PDF](#))

AUTHOR INFORMATION

Corresponding Author

Byoung Don Kong – Pohang University of Science and Technology (POSTECH), Pohang, Gyeongsangbuk-do 37673, Republic of Korea; orcid.org/0000-0003-4072-4399; Email: bdkong@postech.ac.kr

Authors

Yeong Jin Ahn – Pohang University of Science and Technology (POSTECH), Pohang, Gyeongsangbuk-do 37673, Republic of Korea

Yun Ho Lee – Pohang University of Science and Technology (POSTECH), Pohang, Gyeongsangbuk-do 37673, Republic of Korea

Su Hyun Park – Pohang University of Science and Technology (POSTECH), Pohang, Gyeongsangbuk-do 37673, Republic of Korea

Jeong Wook Kim – Pohang University of Science and Technology (POSTECH), Pohang, Gyeongsangbuk-do 37673, Republic of Korea

Cheul Hyun Yoon – Pohang University of Science and Technology (POSTECH), Pohang, Gyeongsangbuk-do 37673, Republic of Korea

Seongjun Kim – National Institute for Nanomaterials Technology (NINT), Pohang University of Science and Technology (POSTECH), Pohang, Gyeongsangbuk-do 37673, Republic of Korea

Young Jae Park – National Institute for Nanomaterials Technology (NINT), Pohang University of Science and Technology (POSTECH), Pohang, Gyeongsangbuk-do 37673, Republic of Korea

Complete contact information is available at:
<https://pubs.acs.org/10.1021/acs.jpcc.Sc03173>

Notes

The authors declare no competing financial interest.

ACKNOWLEDGMENTS

This work has been supported by the Samsung Research Funding and Incubation Center of Samsung Electronics (SRFC-IT2102-01) and National Research Foundation (NRF) grant funded by the Korea government (Ministry of Science and ICT) (NRF-2021M3F3A2A03017770, 2022-0-00720-002, and RS-2023-00266246)

REFERENCES

- Millan, J.; Godignon, P.; Perpina, X.; Perez-Tomas, A.; Rebollo, J. A Survey of Wide Bandgap Power Semiconductor Devices. *IEEE Trans. Power Electron.* **2014**, *29*, 2155–2163.
- Biela, J.; Schweizer, M.; Waffler, S.; Kolar, J. W. SiC versus Si—Evaluation of Potentials for Performance Improvement of Inverter and DC–DC Converter Systems by SiC Power Semiconductors. *IEEE Trans. Ind. Electron.* **2011**, *58*, 2872–2882.
- Nakamura, T.; Sasagawa, M.; Nakano, Y.; Otsuka, T.; Miura, M. Large Current SiC Power Devices for Automobile Applications. In *The 2010 International Power Electronics Conference-ECCE ASIA*; IEEE: **2010**, 1023–1026.
- Brown, D. M.; Downey, E.; Ghezzo, M.; Kretchmer, J.; Krishnamurthy, V.; Hennessy, W.; Michon, G. Silicon Carbide MOSFET Technology. *Solid-State Electron.* **1996**, *39*, 1531–1542.
- Stevanovic, L. D.; Matocha, K. S.; Losee, P. A.; Glaser, J. S.; Nasadoski, J. J.; Arthur, S. D. Recent Advances in Silicon Carbide MOSFET Power Devices. In *2010 Twenty-Fifth Annual IEEE Applied Power Electronics Conference and Exposition (APEC)*; IEEE: **2010**, 401–407.
- Deák, P.; Knaup, J. M.; Hornos, T.; Thill, C.; Gali, A.; Frauenheim, T. The Mechanism of Defect Creation and Passivation at the SiC/SiO₂ Interface. *J. Phys. D: Appl. Phys.* **2007**, *40*, 6242–6253.
- Knaup, J. M.; Deák, P.; Frauenheim, Th.; Gali, A.; Hajnal, Z.; Choyke, W. J. Defects in SiO₂ as the Possible Origin of Near Interface Traps in the SiC/SiO₂ System: A Systematic Theoretical Study. *Phys. Rev. B* **2005**, *72*, No. 115323.
- Shen, X.; Pantelides, S. T. Identification of a Major Cause of Endemically Poor Mobilities in SiC/SiO₂ Structures. *Appl. Phys. Lett.* **2011**, *98*, No. 053507.
- Devynck, F.; Alkauskas, A.; Broqvist, P.; Pasquarello, A. Defect Levels of Carbon-Related Defects at the SiC/SiO₂ Interface from Hybrid Functionals. *Phys. Rev. B* **2011**, *83*, No. 195319.
- Kobayashi, T.; Matsushita, Y. I. Structure and Energetics of Carbon Defects in SiC (0001)/SiO₂ Systems at Realistic Temperatures: Defects in SiC, SiO₂, and at Their Interface. *J. Appl. Phys.* **2019**, *126*, 145302.
- Tersoff, J. New Empirical Approach for the Structure and Energy of Covalent Systems. *Phys. Rev. B* **1988**, *37*, 6991–7000.
- Tersoff, J. Modeling Solid-State Chemistry: Interatomic Potentials for Multicomponent Systems. *Phys. Rev. B* **1989**, *39*, 5566–5568.
- Tersoff, J. Chemical Order in Amorphous Silicon Carbide. *Physical Review B* **1994**, *49*, 16349–16352.

- (14) Munetoh, S.; Motooka, T.; Moriguchi, K.; Shintani, A. Interatomic Potential for Si–O Systems Using Tersoff Parameterization. *Comput. Mater. Sci.* **2007**, *39*, 334–339.
- (15) de Brito Mota, F.; Justo, J. F.; Fazzio, A. Hydrogen Role on the Properties of Amorphous Silicon Nitride. *J. Appl. Phys.* **1999**, *86*, 1843–1847.
- (16) Kinaci, A.; Haskins, J. B.; Sevik, C.; Çağın, T. Thermal Conductivity of BN-C Nanostructures. *Phys. Rev. B* **2012**, *86*, No. 115410.
- (17) Narayanan, B.; Chan, H.; Kinaci, A.; Sen, F. G.; Gray, S. K.; Chan, M. K. Y.; Sankaranarayanan, S. K. R. S. Machine Learnt Bond Order Potential to Model Metal–Organic (Co–C) Heterostructures. *Nanoscale* **2017**, *9*, 18229–18239.
- (18) Chan, H.; Sasikumar, K.; Srinivasan, S.; Cherukara, M.; Narayanan, B.; Sankaranarayanan, S. K. R. S. Machine Learning a Bond Order Potential Model to Study Thermal Transport in WSe₂ Nanostructures. *Nanoscale* **2019**, *11*, 10381–10392.
- (19) Koneru, A.; Batra, R.; Manna, S.; Loeffler, T. D.; Chan, H.; Sternberg, M.; Avarca, A.; Singh, H.; Cherukara, M. J.; Sankaranarayanan, S. K. R. S. Multi-Reward Reinforcement Learning Based Bond-Order Potential to Study Strain-Assisted Phase Transitions in Phosphorene. *J. Phys. Chem. Lett.* **2022**, *13*, 1886–1893.
- (20) Hammerschmidt, T.; Kratzer, P.; Scheffler, M. Analytic Many-Body Potential for InAs/GaAs Surfaces and Nanostructures: Formation Energy of InAs Quantum Dots. *Phys. Rev. B* **2008**, *77*, No. 235303.
- (21) Luo, Y.-R. *Comprehensive Handbook of Chemical Bond Energies*; CRC Press: Boca Raton, FL, 2007.
- (22) Thompson, A. P.; Aktulga, H. M.; Berger, R.; Bolintineanu, D. S.; Brown, W. M.; Crozier, P. S.; in't Veld, P. J.; Kohlmeyer, A.; Moore, S. G.; Nguyen, T. D.; et al. LAMMPS – A Flexible Simulation Tool for Particle-Based Materials Modeling at the Atomic, Meso, and Continuum Scales. *Comput. Phys. Commun.* **2022**, *271*, No. 108171.
- (23) Kroll, P.; Milko, M. Theoretical Investigation of the Solid State Reaction of Silicon Nitride and Silicon Dioxide Forming Silicon Oxynitride (Si₂N₂O) under Pressure. *Z. Anorg. Allg. Chem.* **2003**, *629*, 1737–1750.
- (24) Srinivasa, S. R.; Cartz, L.; Jorgensen, J. D.; Worlton, T. G.; Beyerlein, R. A.; Billy, M. High-Pressure Neutron Diffraction Study of Si₂N₂O. *J. Appl. Crystallogr.* **1977**, *10*, 167–171.
- (25) Hanwell, M. D.; Curtis, D. E.; Lonie, D. C.; Vandermeersch, T.; Zurek, E.; Hutchison, G. R. Avogadro: An Advanced Semantic Chemical Editor, Visualization, and Analysis Platform. *J. Cheminf.* **2012**, *4*, 17.
- (26) Nosé, S. A Unified Formulation of the Constant Temperature Molecular Dynamics Methods. *J. Chem. Phys.* **1984**, *81*, 511–519.
- (27) Hoover, W. G. Canonical Dynamics: Equilibrium Phase-Space Distributions. *Phys. Rev. A* **1985**, *31*, 1695–1697.
- (28) Maghfiroh, C. Y.; Arkundato, A.; Misto, Maulina, W. Parameters (σ , ϵ) of Lennard-Jones for Fe, Ni, Pb for Potential and Cr Based on Melting Point Values Using the Molecular Dynamics Method of the LAMMPS Program. *J. Phys.: Conf. Ser.* **2020**, *1491*, No. 012022.
- (29) Lyulin, S. V.; Larin, S. V.; Gurtovenko, A. A.; Nazarychev, V. M.; Falkovich, S. G.; Yudin, V. E.; Svetlichnyi, V. M.; Gofman, I. V.; Lyulin, A. V. Thermal Properties of Bulk Polyimides: Insights from Computer Modeling versus Experiment. *Soft Matter* **2014**, *10*, 1224.
- (30) Song, Y.; Dhar, S.; Feldman, L. C.; Chung, G.; Williams, J. R. Modified Deal Grove Model for the Thermal Oxidation of Silicon Carbide. *J. Appl. Phys.* **2004**, *95*, 4953–4957.
- (31) Lager, G. A.; Jorgensen, J. D.; Rotella, F. J. Crystal Structure and Thermal Expansion of α -Quartz SiO₂ at Low Temperatures. *J. Appl. Phys.* **1982**, *53*, 6751–6756.
- (32) Rustad, J. R.; Yuen, D. A.; Spera, F. J. Molecular Dynamics of Liquid SiO₂ under High Pressure. *Phys. Rev. A* **1990**, *42*, 2081–2089.
- (33) Chanthaphan, A.; Hosoi, T.; Shimura, T.; Watanabe, H. Study of SiO₂/4H-SiC Interface Nitridation by Post-Oxidation Annealing in Pure Nitrogen Gas. *AIP Adv.* **2015**, *5*, No. 097134.
- (34) Kim, C.; Moon, J. H.; Yim, J. H.; Lee, D. H.; Lee, J. H.; Lee, H. H.; Kim, H. J. Comparison of Thermal and Atomic-Layer-Deposited Oxides on 4H-SiC after Post-Oxidation-Annealing in Nitric Oxide. *Appl. Phys. Lett.* **2012**, *100*, No. 082112.
- (35) Renz, A. B.; Vavasour, O. J.; Gammon, P. M.; Li, F.; Dai, T.; Antoniou, M.; Baker, G. W. C.; Bashar, E.; Grant, N. E.; Murphy, J. D.; et al. The Improvement of Atomic Layer Deposited SiO₂/4H-SiC Interfaces via a High Temperature Forming Gas Anneal. *Mater. Sci. Semicond. Process.* **2021**, *122*, No. 105527.
- (36) Chung, G. Y.; Tin, C. C.; Williams, J. R.; McDonald, K.; Di Ventra, M.; Pantelides, S. T.; Feldman, L. C.; Weller, R. A. Effect of Nitric Oxide Annealing on the Interface Trap Densities near the Band Edges in the 4H Polytype of Silicon Carbide. *Appl. Phys. Lett.* **2000**, *76*, 1713–1715.
- (37) Soler, J. M.; Artacho, E.; Gale, J. D.; García, A.; Junquera, J.; Ordejón, P.; Sánchez-Portal, D. The SIESTA Method for Ab Initio Order-N Materials Simulation. *J. Phys.: Condens. Matter* **2002**, *14*, 2745–2779.
- (38) Troullier, N.; Martins, J. L. Efficient Pseudopotentials for Plane-Wave Calculations. *Phys. Rev. B* **1991**, *43*, 1993–2006.
- (39) Alkauskas, A.; Broqvist, P.; Pasquarello, A. Defect Levels through Hybrid Density Functionals: Insights and Applications. *Phys. Status Solidi B* **2011**, *248*, 775–789.
- (40) Perdew, J. P.; Ernzerhof, M.; Burke, K. Rationale for Mixing Exact Exchange with Density Functional Approximations. *J. Chem. Phys.* **1996**, *105*, 9982–9985.
- (41) Perdew, J. P.; Ernzerhof, M.; Zupan, A.; Burke, K. Nonlocality of the Density Functional for Exchange and Correlation: Physical Origins and Chemical Consequences. *J. Chem. Phys.* **1998**, *108*, 1522–1531.
- (42) Schimka, L.; Harl, J.; Kresse, G. Improved Hybrid Functional for Solids: The HSEsol Functional. *J. Chem. Phys.* **2011**, *134*, No. 024116.
- (43) Yakovkin, I. N.; Dowben, P. A. The Problem of the Band Gap in LDA Calculations. *Surf. Rev. Lett.* **2007**, *14*, 481–487.
- (44) Afanasev, V. V.; Bassler, M.; Pensl, G.; Schulz, M. Intrinsic SiC/SiO₂ Interface States. *Phys. Status Solidi A* **1997**, *162*, 321–337.
- (45) Andersen, A. M. Structural Studies of Metabolic Products of Dopamine. III. Crystal and Molecular Structure of (−)-Adrenaline. *Acta Chem. Scand., Ser. B* **1975**, *29*, 239–244.
- (46) Gelest Inc. Trimethylsilane: Safety Data Sheet; SIT8570.0, 2015.
- (47) Bates, O. K. Thermal Conductivity of Liquid Silicones. *Ind. Eng. Chem.* **1949**, *41*, 1966–1968.
- (48) Laxman, R.; Hendricks, N. H.; Arkles, B. Synthesizing Low-k CVD Materials for Fab Use. *Semicond. Int.* **2000**, *23*, 95–99.
- (49) Andrianov, K. A.; Slonimskii, G. L.; Zhdanov, A. A.; Yu. Levin, V.; Godovskii, Y. K.; Moskalenko, V. A. Some Physical Properties of Polyorganosiloxanes. I. Linear Polyorganosiloxanes. *J. Polym. Sci., Part A: Polym. Chem.* **1972**, *10*, 1–22.
- (50) Volkov, A. Polydimethylsiloxane (PDMS). In *Encyclopedia of Membranes*; Springer, Berlin, Heidelberg, 2013, 1–2. DOI: .